J. Fluid Mech. (1984), *vol.* 147, *pp.* 53–79
Printed in Great Britain

Heat- and fluid-flow phenomena in weld pools

By G. M. OREPER AND J. SZEKELY

Department of Materials Science and Engineering, Massachusetts Institute of Technology, Cambridge, Massachusetts 02139 USA

(Received 3 May 1982 and in revised form 9 April 1984)

A mathematical formulation is presented for the transient development of the fluid-flow field and the temperature field in a liquid pool, generated by a spatially variable heat flux falling on an initially solid metal block. This physical situation is an idealized representation of a TIG (tungsten–inert-gas) welding process. In the formulation allowance is made for electromagnetic, buoyancy and surface forces and the resultant equations are solved numerically.

It is found that both the convective flow field and the temperature field are markedly affected by the nature of the heat flux and the flux of electric current falling on the free surface.

In the absence of surface-tension effects a broadly distributed heat flux and corresponding current distribution cause a situation where both electromagnetic and buoyancy forces are important in determining the fluid-flow field; however, in these systems the fluid-flow field does not play a significant role in defining the heat-transfer process. In contrast, a sharply focused heat flux and current density on the free surface give rise to strong electromagnetically driven flows, which play an important role in determining the shape of the weld pool.

Calculations are also done exploring the effect of surface-tension-driven flows. It is found that surface-tension gradients may produce quite high surface velocities and can have a profound effect on determining the weld-pool shape.

1. Introduction

In recent years there has been a growing recognition of the fact that fluid motion in weld pools may play an important role in affecting both the heat-transfer phenomena and ultimately the mechanical properties of the welds produced. In the metallurgical literature useful work has been published on fluid-flow and heat-transfer problems in electroslag welding systems and in the related area of electroslag refining (Dilawari, Szekely & Eagar 1978; Choudhary & Szekely 1980); however, fluid-flow problems in arc (TIG, tungsten–inert-gas) welding systems have received rather less attention up to the present.

Figure 1 (*a*) shows a sketch of a typical TIG welding system, where it is seen that an arc is being struck between an inert electrode and a molten weld pool. The thermal energy generated in the arc causes the base metal to melt. The solidification of the molten metal in the weld pool forms the bond between the two pieces that are joined by the process.† A somewhat idealized representation of the system is sketched in figure 1 (*b*), depicting transient heat flow and fluid flow in a metal pool, formed on an initially solid metal block, by the action of an impinging plasma jet.

On inspection of figure 1 (*b*) it is seen that this problem has the following key physical components.

† A good description of the TIG system is available in the monograph of Lancaster (1980).

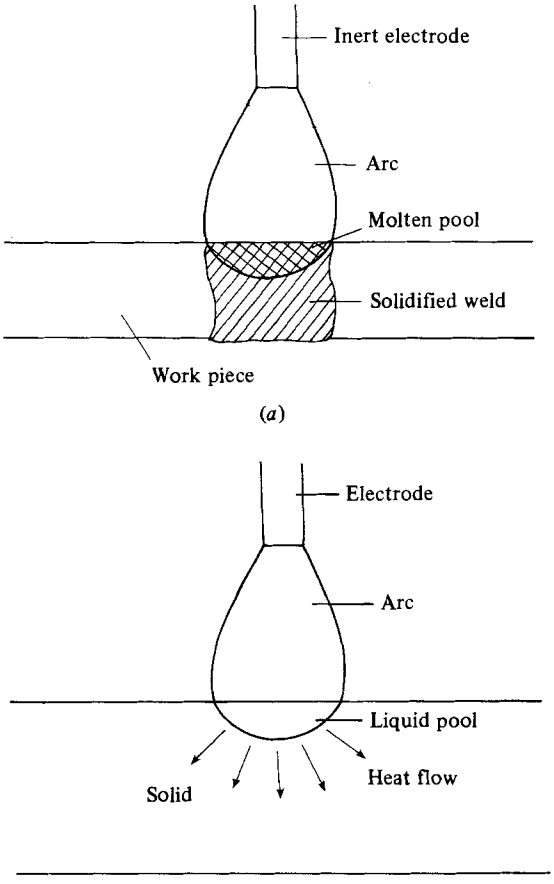

FIGURE 1. (*a*) Sketch of the TIG welding system. (*b*) Idealized representation of the welding process.

(1) The plasma jet impinging onto the surface of the metal pool acts both as a distributed heat flux falling on the surface and as the source of a spatially non-uniform current that passes through the pool.

(2) The passage of the current through the pool gives rise to an electromagnetic force field, owing to its interaction with the magnetic field thus generated; this force field produces a recirculating motion in the pool.

(3) The temperature differences in the pool give rise to a buoyancy field, which also generates motion (more precisely the motion results from the combined action of these two body force fields).

(4) Surface-tension gradients at the free surface and the shear stress exerted by the impinging plasma jet may constitute additional driving forces for the flow, and in extreme cases may also cause the deformation of the free surface.

(5) The convective and conductive heat-transfer processes in the pool cause the melting of the block, through the lateral advancement of the melt–solid interface.

Ideally a comprehensive model of a welding process will have to take into account all these factors. The work to be described in this paper was undertaken to provide an improved basic understanding of the heat- and the fluid-flow phenomena in this system, with the ultimate objective of using the results obtained for the solution of problems in welding technology.

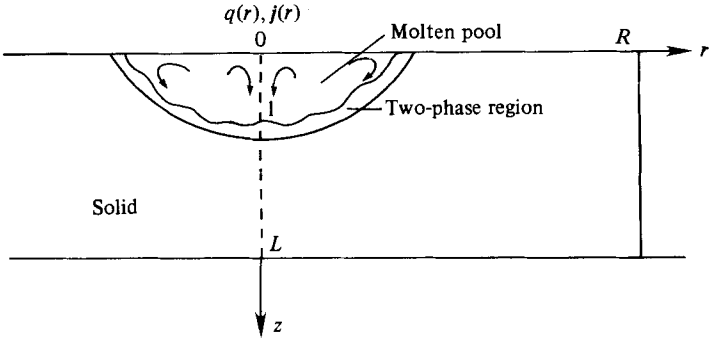

FIGURE 2. Sketch of the system used in the computations.

In the development of the formulation the effects (1)–(4) were considered, although the study of surface deformation and the shear exerted by the impinging plasma jet has been deferred at this stage. As will be seen, this formulation does appear to represent a significant advance over what has been available up to the present.

Previous work

While the precise problem defined above has not yet been tackled, a great deal of useful work has been reported in the literature on various components of this rather complex problem.

Transient melting or solidification in the presence of liquid-phase convection has been studied by a number of investigators. In this regard, particularly noteworthy is the elegant numerical work of Sparrow, Pantankar & Ramadhyani (1977), who considered the progressive enlargement of a cavity due to natural convection.

Perhaps the closest approach to the specific weld-pool problem has been that of Atthey (1980), who examined the steady-state laminar electromagnetically driven flow in a cavity of predetermined dimensions, and for a predetermined electromagnetic force field – for an isothermal system.

The problem to be tackled as part of the work to be reported here differs from these earlier investigations, because in the formulation allowance will be made for: (i) the combined effects of the electromagnetic buoyancy and surface-tension forces; (ii) the unsteady-state nature of the problem.

2. Formulation

Figure 2 shows a schematic sketch of the system, which is seen to consist of a solid plate containing a liquid pool. As indicated in the sketch, a spatially distributed heat flux and current fall on the free surface corresponding to the $z = 0$ plane. As a result, circulation is induced in the pool, and the associated heat transfer will cause the boundaries of the pool to expand.

The quantitative representation of this system will have the following components:

(1) the electromagnetic force field has to be evaluated;

(2) the temperature distribution has to be calculated, together with the time-dependent position of the melt–solid boundary;

(3) the fluid-flow field has to be obtained.

This is an inherently transient problem and these three sets of equations are coupled, because fluid flow affects convective heat transfer, while the fluid flow itself is driven by the combined action of the electromagnetic, buoyancy and surface tension forces.

It follows that the problem has to be stated by expressing Maxwell's equations, the Navier–Stokes equations and the differential thermal-energy balance equation; in the latter due allowance has to be made for convection in the pool and the absorption of the latent heat of melting.

Heat transfer

As sketched in figure 2, three distinct domains have to be considered in representing the heat-transfer process:

(i) the molten phase, where both conduction and convection are of importance;

(ii) the two-phase or mushy regions, where the latent heat of melting is absorbed;

(iii) the solid region, where heat is transmitted by conduction only.

In the statement of the governing equations in a dimensionless form it is desirable to work in terms of normalized quantities, which in turn requires that the proper scales be defined for the key dependent and independent variables.

Let us define the characteristic timescale as

$$\frac{L^2 C_{p,0}\,\rho}{k_s}\,\frac{1}{St};$$

where

$$St = \frac{C_{p,0}(T_l - T_0)}{\lambda},$$

which follows from the heat balance at the moving boundary. Here $L \equiv$ thickness of the plate (see figure 2), $C_{p,0} \equiv$ specific heat of the material, $k_s \equiv$ thermal conductivity of the solid, $\rho \equiv$ density, $T_l \equiv$ liquidus temperature, $T_0 \equiv$ initial temperature and $\lambda \equiv$ heat of fusion. The timescale chosen corresponds to the melting time, which includes the Stefan number St. When the Stefan number is of the order of unity, this melting time will be similar to the timescale for thermal diffusion. In the present case St is of the order of 3–4 so that these two timescales would be of similar magnitude.

In defining the lengthscale different values have to be chosen for heat transfer and fluid flow since fluid will be confined to the weld pool. For fluid flow the characteristic lengthscales are L_R and L_Z, corresponding to the pool radius and the pool depth respectively.

On designating the aspect ratio as $A = L_Z/L_R$ and using the equation of continuity, the characteristic velocities are related by

$$U_{Z,0} = A U_{R,0}.$$

Using these scaling factors, the dimensionless vorticity r may be written as

$$\xi = \frac{1}{r}\frac{\partial U_R}{\partial z} - \frac{A^2}{r}\frac{\partial U_Z}{\partial r}.$$

When A is small, as is the case for most welding situations, the second term in this expression will be small.

The appropriate scales for the stream function ψ are related by

$$\rho U_{Z,0} L_R^2 = \rho U_{R,0} L_Z L_R.$$

Then the dimensionless form of the vorticity-transport equation may be written as

$$\frac{r^3}{A^2\,Re\,Pr}\frac{1}{k}\frac{L_z^2}{L^2}\frac{\partial\xi}{\partial t}+r^2\left[\frac{\partial}{\partial z}(\xi U_Z r)+\frac{\partial}{\partial r}(\xi U_R r)\right]$$
$$-\frac{1}{Re\,A^2}\frac{\partial}{\partial z}\left(r^3\frac{\partial\xi}{\partial z}\right)-\frac{1}{Re}\frac{\partial}{\partial r}\left(r^3\frac{\partial\xi}{\partial r}\right)-\frac{Gr\,A}{Re^2}\frac{\partial\theta}{\partial r}\frac{T_1-T_0}{\Delta T}-\text{curl}\,\boldsymbol{F}_e=0 \quad (1)$$

where

the Reynolds number, $Re=\dfrac{\rho U_{R,0}L_R}{\mu}$,

the Prandtl number, $Pr=\dfrac{C_{p,0}\mu}{k_1}$,

the Grashof number, $Gr=\dfrac{g\beta L_R^3\Delta T\rho^2}{\mu^2}$,

the dimensionless thermal conductivity $k=$ thermal conductivity$/k_s$, ΔT is the maximum temperature difference in the weld pool, μ is the viscosity,

the dimensionless temperature, $\theta=\dfrac{T-T_0}{T_1-T_0}$,

r and z are the dimensionless radial and axial coordinates, and curl $\boldsymbol{F}_e$ is the dimensionless curl of electromagnetic force, to be defined subsequently; subscripts l and s refer to the liquid and solid phases respectively.

The stream function ψ, which appears in the thermal-energy balance equation, may be related to the vorticity by

$$\frac{1}{A^2}\frac{\partial}{\partial z}\left(\frac{1}{r}\frac{\partial\psi}{\partial z}\right)+\frac{\partial}{\partial r}\left(\frac{1}{r}\frac{\partial\psi}{\partial r}\right)+r\xi=0. \quad (2)$$

The differential thermal-energy balance equation takes the following form:

$$St\,r\frac{\partial\theta}{\partial t}+Re\frac{L_z}{L}Pr\,k\left[\frac{\partial}{\partial z}\left(\theta\frac{\partial\psi}{\partial z}\right)-\frac{\partial}{\partial r}\left(\theta\frac{\partial\psi}{\partial z}\right)\right]-\frac{1}{C_p}\left[\frac{\partial}{\partial z}\left(kr\frac{\partial\theta}{\partial z}\right)+\frac{\partial}{\partial z}\left(kr\frac{\partial\theta}{\partial r}\right)\right]=0, \quad (3)$$

where $C_p\equiv$ dimensionless specific heat, i.e. specific heat$/C_{p,0}$. Equation (3) will be valid for all three regions, with the stream function being zero in the mushy region and in the solid phase.

In order to allow for the release of the latent heat in the mushy region, the following dimensionless expression was used to represent the specific heat:

$$C_p=\frac{1}{St\,\Delta\theta_{ls}}, \quad (4)$$

where $\Delta\theta_{ls}=\theta_l-\theta_s$ is the temperature range of melting, and θ_s is the solidus temperature of the metal. It should be noted, furthermore, that the thermal conductivity in the mushy zone was assumed to vary linearly between the values for the molten and the solid regions.

The technique of using an effective specific heat to represent the absorption of a latent heat of phase change is frequently employed in melting or solidification problems (Szekely 1979).

The last two terms on the left-hand side of (1) represent the buoyancy and the electromagnetic forces respectively.

The boundary conditions for (1) and (2) take the following form:

$$\frac{\partial \xi}{\partial r} = 0 \quad \text{at} \quad r = 0,$$

$$\xi = 0 \quad \text{at} \quad z = 0,$$

$$\psi = 0 \quad \text{along all boundaries,}$$

which in physical terms specify that the gradient of the vorticity/r has to be zero at the free surface and at the axis of symmetry. The expression used for specifying the vorticity at the melt–solid interface, i.e. at the moving boundary, will be given subsequently.

The boundary conditions associated with (3) take the following form:

$$-\frac{k_1(T_1 - T_0)}{q_0 L}\frac{\partial \theta}{\partial z} = \bar{q}(r) \quad \text{at} \quad z = 0,$$

$$\frac{\partial \theta}{\partial z} = 0 \quad \text{at} \quad z = 1,$$

$$\frac{\partial \theta}{\partial r} = 0 \quad \text{at} \quad r = 0,$$

$$\theta = 0 \quad \text{at} \quad r = \frac{R}{L},\dagger$$

where $\bar{q}(r) = q(r)/q_0$ is the dimensionless heat flux from the arc falling on the free surface of the metal, and q_0 is the heat flux at the axis of symmetry.

When there is a surface-tension gradient at the free surface, caused by the temperature dependence of the interfacial tension, the boundary condition for vorticity has to take the following form:

$$\xi = \frac{M}{Re}\frac{1}{r}\frac{\partial \theta}{\partial r} \quad \text{at} \quad z = 0, \tag{5}$$

where

$$M = \frac{\rho L_Z \Delta T \dfrac{\partial \gamma}{\partial T}}{\mu^2}$$

is the surface-tension parameter and γ is the interfacial tension. The quantity M may also be regarded as a surface-tension Reynolds number (Ostrach 1979).

Calculation of the electromagnetic force field

In order to calculate $\boldsymbol{F}_e$, which appeared as one of the driving forces in (1), let us define an electromagnetic stream function ψ_e as

$$\boldsymbol{j} = \operatorname{curl}\left(\frac{\psi_e}{r}\boldsymbol{e}_\phi\right), \tag{6}$$

where $\boldsymbol{j}$ is the electric current density. Then for small values of the magnetic Reynolds number $Re_m \ll 1$ one may obtain the following relationship:

$$\frac{\partial}{\partial z}\left(\frac{1}{\sigma r}\frac{\partial \psi_e}{\partial z}\right) + \frac{\partial}{\partial r}\left(\frac{1}{\sigma r}\frac{\partial \psi_e}{\partial r}\right) = 0. \tag{7}$$

† An additional constraint was also introduced that the temperature of the free surface may not exceed the upper value corresponding to the temperature when heat loss by vaporization equals the incident heat flux. As a practical matter this value is at least 500 K below the boiling point.

Here $Re_m = \mu_e \sigma U_{R,0} L_R$, μ_e is the magnetic permeability and σ is the electric conductivity.

When $Ha^2/Re \ll 1$, curl $\boldsymbol{F}_e$ may be expressed as

$$\frac{Re_j}{Re^2} \frac{L_R^3 L_Z}{L^3} r^2 \operatorname{curl} (\boldsymbol{j} \times \boldsymbol{B}). \tag{8}$$

Here B is the dimensionless magnetic induction, $\boldsymbol{j}$ is a dimensionless electric current density.

$H_a = B_0 L_R (\sigma/\mu)^{\frac{1}{2}}$ is the Hartmann number, $B_0 = \mu_e j_0 L$ is the characteristic magnetic induction, j_0 is the scale of the electric current density, and $Re_j = \mu_e j_0^2 L^4 \rho/\mu^2$.

The boundary conditions for the electromagnetic field equations take the following form:

$$\psi_e(r) = \int_0^r j_z r \, dr \quad \text{at} \quad z = 0, \quad \psi_e = 0 \quad \text{at} \quad z = L, \tag{9}$$

$$\psi_e = 0 \quad \text{at} \quad r = 0, \quad \psi_e = \psi_e|_{z=0}(1-z) \quad \text{at} \quad r = R, \tag{10}$$

since $\partial j_r/\partial z = 0$. Here $j_z = j_0 \exp(-\alpha_j r)$, the arc-current density falling on the free surface. Equations (1)–(10) then represent the complete statement of the problem.

In order to evaluate the electromagnetic term in the vorticity-transport equation the distribution of the electromagnetic stream function is needed. Close to the free surface the computed results show that

$$\psi_e \approx \psi_e|_{z=0}\left(1 - \frac{Cz}{L}\right), \tag{11}$$

where $C \approx 8$ for the normal mode distribution, and $C \approx 10$ for the cathode spot mode of operation. Now $\partial\psi_e/\partial z \approx -\psi_e|_{z=0} C/L$. The characteristic value of ψ_e is $j_0 L_e^2$, where $L_e = 1/\alpha_j$. Furthermore, $j_0 \sim I\alpha_j^2/\pi$, where I is the total arc current. Close to the surface of the plate the dependence of ψ_e on the radius can be evaluated from the distribution of the electric current along the surface:

$$\psi_{e,z=0} = \int_0^r j_z r \, dr \approx \frac{I\alpha_j r^2}{2\pi} \quad \text{for} \quad r < \frac{1}{\alpha_j}.$$

then

$$\psi_e \frac{\partial\psi_e}{\partial z} \sim \psi_e^2|_{z=0} \frac{C}{L} \sim \frac{I^2 \alpha_j^4 r^4 C}{2\pi^2 L}.$$

The electromagnetic term in the vorticity transport equation may now be written as

$$\frac{r^2}{U_{R0}^2} L_R L_Z \operatorname{curl} (\boldsymbol{j} \times \boldsymbol{B}) = \frac{Rj_m}{Re^2} \frac{C L_R^4 L_Z \alpha_j^4}{\pi^2 L} \frac{\psi_e}{r} \frac{\partial\psi_e}{\partial z}, \tag{12}$$

where $Rj_m = \mu_e I^2 \rho/\mu^2$.

3. The technique of solution

Equations (1) and (3) are two-dimensional unsteady-state differential equations, while the expressions defining the stream function and the electromagnetic stream function are steady-state relationships. While the actual form of the governing equations (1)–(3) was suitable for scaling and order-of-magnitude interpretation, the form of (1)–(3) handled in the numerical integration was slightly different.

The lengthscale used in the integration of both the vorticity-transport equation and the thermal-energy balance equations was the thickness of the plate, while the reference velocity defined for computational purposes was

$$\tilde{U} = \frac{\mu}{\rho L}(\widetilde{Gr})^{\frac{1}{2}}; \tag{13}$$

where the reference value $\widetilde{Gr}$ of the Grashof number was evaluated using the plate thickness L as the characteristic length. This procedure was convenient for generating numerical results, because a time-dependent lengthscale would have introduced unnecessary complications. In order to obtain a solution, the governing equations were put in a finite-difference form, using a 18×20 grid. It should be noted that a rectangular grid pattern was employed using a variable grid spacing having a larger number of grid points in the vicinity of the melt–solid boundary. The grid structure was redefined at each time step.

This procedure differed somewhat from that adopted by Sparrow *et al.* (1977), who used a coordinate transformation in order to solve a melting problem in a cavity. This alternative procedure required the elimination of certain higher-order terms from the differential equation, which was not necessary in the present case.

The unsteady-state equations for the temperature distribution and vorticity were solved through the use of the 'hopscotch method', detailed descriptions of which are readily available in the computational literature (Gourlay 1970; Gourlay & McGuire 1971).

A technique proposed by Spalding and coworkers (Gosman *et al.* 1969) was used for solving the equations for the stream function and the magnetic stream function. In order to avoid the computational complexities posed by the need to evaluate the vorticity at the melt–solid boundary, the following procedure was adopted for each time step.

(1) By using values of the stream function near the boundary and utilizing the relationship $r\xi = \nabla^2\psi$, the $\xi_{i,j}$ values were evaluated at the points adjacent to the phase boundary.

(2) These $\xi_{i,j}$ were assigned as boundary values, and, with the vorticity equation solved, the $\xi_{i,j}$ in the remainder of the liquid domain were evaluated.

(3) The values of the stream function $\psi_{i,j}$ inside the main region were found from the differential equation for the stream function, with the assumption that $\psi_{i,j}$ are given at the boundary.

(4) The values of the stream function near the boundary then had to be corrected for the known condition of ψ at the boundary. This was done by using the relationship $\partial\psi/\partial r = \partial\psi/\partial z = 0$ at the phase boundary.

4. Results

The calculations were carried out for a fixed set of property values, listed in table 1. Three basic sets of conditions were examined, namely a normal mode type of operation and a cathode spot type of operation, as defined in table 2, and the effect of surface tension. The input parameters, except for surface tension, were taken from Nestor (1962). The current distribution and the heat-flux distribution were expressed respectively as

$$j_z(r) = j_0 \exp(-\alpha_j r),$$

$$q(r) = q_0 \exp(-\alpha_q r^2).$$

$C_p \equiv$ specific heat of molten and solid metal = 753 J kg^{-1} K^{-1}
$K_1 \equiv$ thermal conductivity of molten metal = 15.48 W mK^{-1}
$K_s \equiv$ thermal conductivity of solid metal = 31.39 W mK^{-1}
$L \equiv$ thickness of metal plate = 3.1×10^{-2} m
$R \equiv$ maximum radius of region of calculation = 4.65×10^{-2} m
$T \equiv$ temperature (K)
$T_0 \equiv$ initial temperature of metal = 300 K
$T_l \equiv$ liquidus temperature of metal = 1723 K
$T_s \equiv$ solidus temperature of metal = 1523 K
$\theta = (T-T_0)/(T_l-T_0) \equiv$ dimensionless temperature
$\beta \equiv$ coefficient of thermal expansion = 10^{-4} K^{-1}
$\lambda \equiv$ latent heat of fusion = 247 kJ kg^{-1}
$\mu \equiv$ viscosity of molten metal = 0.006 kg m^{-1} s^{-1}
$\mu_e \equiv$ magnetic permeability of free space = 1.26×10^{-6} H m^{-1}
$\rho \equiv$ density of molten and solid metal = 7.2×10^3 kg m^{-3}
$\sigma \equiv$ electrical conductivity, 7.14×10^5 Ω^{-1} m^{-1}

TABLE 1. Physical-property values used in the computation

Parameter	Normal mode	Cathode spot mode
q_0	2.2×10^7 W m^{-2}	6.135×10^7 W m^{-2}
α_q	3.18×10^4 m^{-2}	1×10^5 m^{-2}
j_0	1.9×10^6 A m^{-2}	5.11×10^6 A m^{-2}
α_j	1.3×10^2 m^{-1}	2.3×10^2 m^{-1}

TABLE 2. The parameters used to characterize the heat-flux and electric-current distribution on the surface

The 'normal mode' gave a relatively diffuse current and heat-flow distribution, while the 'cathode spot' type of operation represented a more sharply focused input of current and thermal energy. As will be shown subsequently, these two different modes of operation will tend to produce markedly different behaviour.

The third group of results presented provides a preliminary examination of the role played by surface-tension-driven flows. Before proceeding with the actual presentation of the computed results, we note that, wherever possible, advantage will be taken of the insights that may be developed from the examination of the dimensionless form of the governing equations.

4.1. *The normal mode of operation*

In examining this system, ideally one would wish to obtain insight regarding the following questions:

(i) whether the flow is driven primarily by buoyancy or electromagnetic forces;

(ii) whether the heat- and fluid-flow phenomena are 'in phase';

(iii) whether convection plays an important role in affecting the heat-transfer process.

Let us define the ratio of the electromagnetic force to buoyancy:

$$R = \frac{Rj_m CL_R^4 L_Z \alpha_j^4}{Gr A}. \tag{14}$$

R may also be written as

$$R = \frac{\mu_e I^2 C L_R^2 \alpha_j^4}{\rho \pi^2 L g \beta \Delta T}.$$

For $L_R = 5 \times 10^{-3}$ m, which is a typical weld-pool radius in many applications, $R \approx 0.3$. In the early stages of the process, when L_R is small, buoyancy is more important than electromagnetic forces. It is also seen that R depends very strongly on the distribution of the electric current α_j^4 over the surface and on the thickness L of the plate.

Since the buoyancy term is proportional to $\partial\theta/\partial r$, and the steepest temperature gradients will be at the outer edge of the weld pool at the melt–solid interface, one would expect buoyancy-driven flow to dominate there throughout. When $R < 1$ and $Re\,A^2 \ll 1$, $R \sim Gr\,A^3$; hence

$$U_{R,0} \sim \frac{g\beta \Delta T L_Z^3 \rho}{\mu L_R}. \tag{15}$$

In contrast, when $Re\,A^2 > 1$, $Re \sim (Gr\,A)^{\frac{1}{2}}$; hence $U_{R,0} \sim (gL_Z \beta \Delta T)^{\frac{1}{2}}$. It is thus seen that the relationship between $U_{R,0}$ and the other process parameters is extremely sensitive to the scale used. Therefore, as will be discussed in the presentation of the computed results, the main utility of the order-of-magnitude approach will be interpretive, rather than predictive in this instance.

Upon considering the vorticity-transport equation (1) it is readily seen that the coefficient of the transient term

$$\frac{St}{Re\,A^2\,Pr}\frac{L_Z^2}{L^2} \ll 1. \tag{16}$$

It follows that the transient term may be neglected and that the velocity field will be in phase with the temperature field. Stated in other words, while the velocity field will obviously be time-dependent, this will be caused by changes in the temperature field and the system geometry. This is an interesting behaviour for a low-Prandtl-number system, which will be discussed subsequently.

Upon considering the thermal-energy balance equation (3) it is seen that the convective transport terms are multiplied by the factor

$$Re\frac{L_Z}{L} Pr\,k, \tag{17}$$

which at least in the initial stages, when L_Z is small, may be much less than unity. Under these conditions convection does not play an important role in heat transfer, which is dominated by transient conduction.

Turning to the computed results, figures 3 (*a*)–(*c*) show the progressive development of the temperature profiles calculated by considering conductive heat transfer only. The development of the molten-metal pool is readily seen by following the $\theta = 1$ isotherm, which defines the melt line.

Figures 4 (*a*)–(*c*) show the computed temperature profiles for the case where allowance has been made for convection and both electromagnetic and buoyancy forces are taken into consideration. This plot is similar to that shown earlier in figure 3, but there are some slight differences, which will be discussed subsequently.

Figures 5 (*a*)–(*c*) show plots of the computed velocity fields corresponding to the temperatures shown in figure 4 for various values of time. Initially the flow appears to be dominated by buoyancy forces, but subsequently two circulating loops are

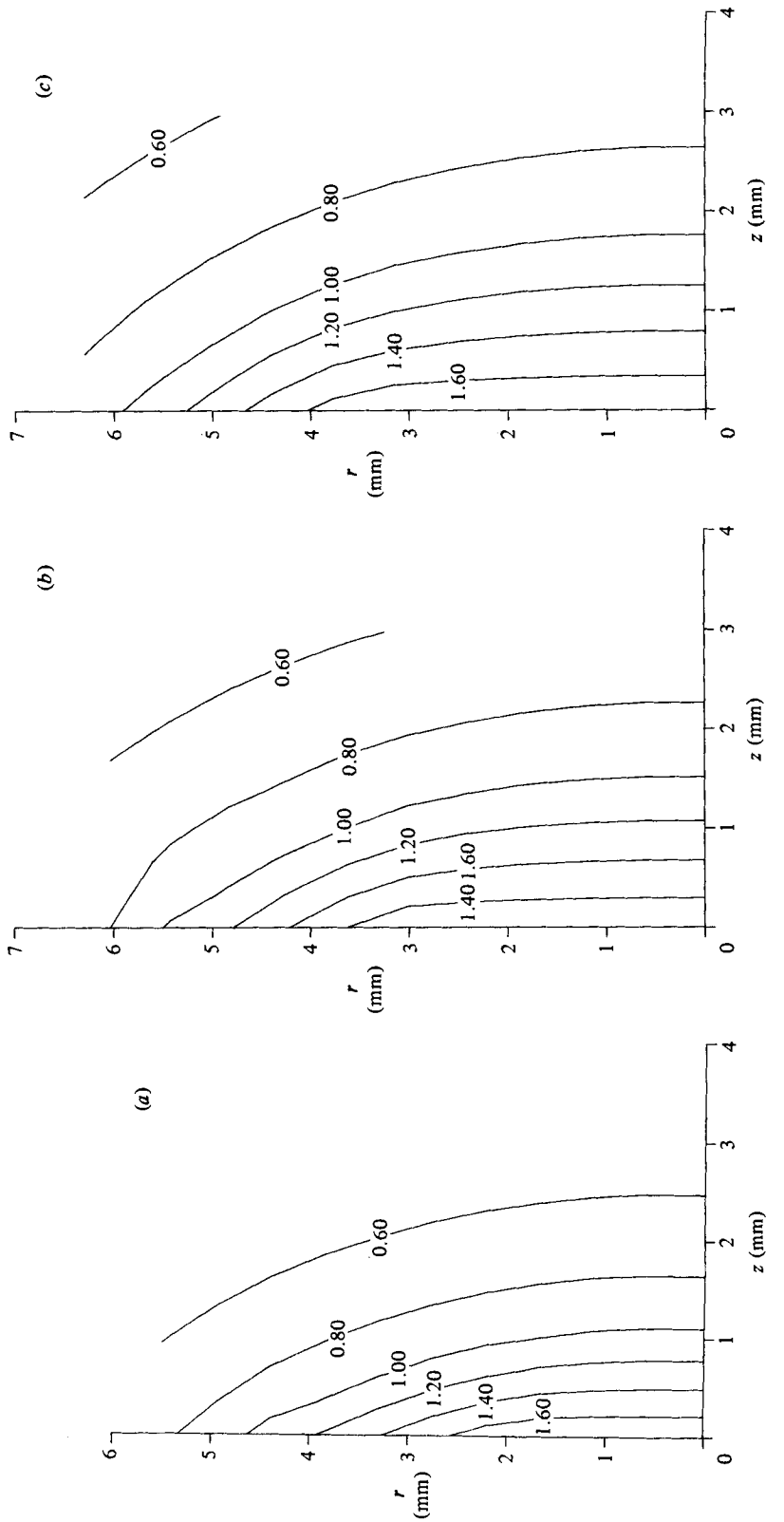

FIGURE 3. Temperature distribution for purely conductive heat transfer (normal mode): (*a*) at *t* 2.5 s; (*b*) 5 s; (*c*) 8 s. The numbers on the curves represent the ratio of actual temperature/characteristic temperature.

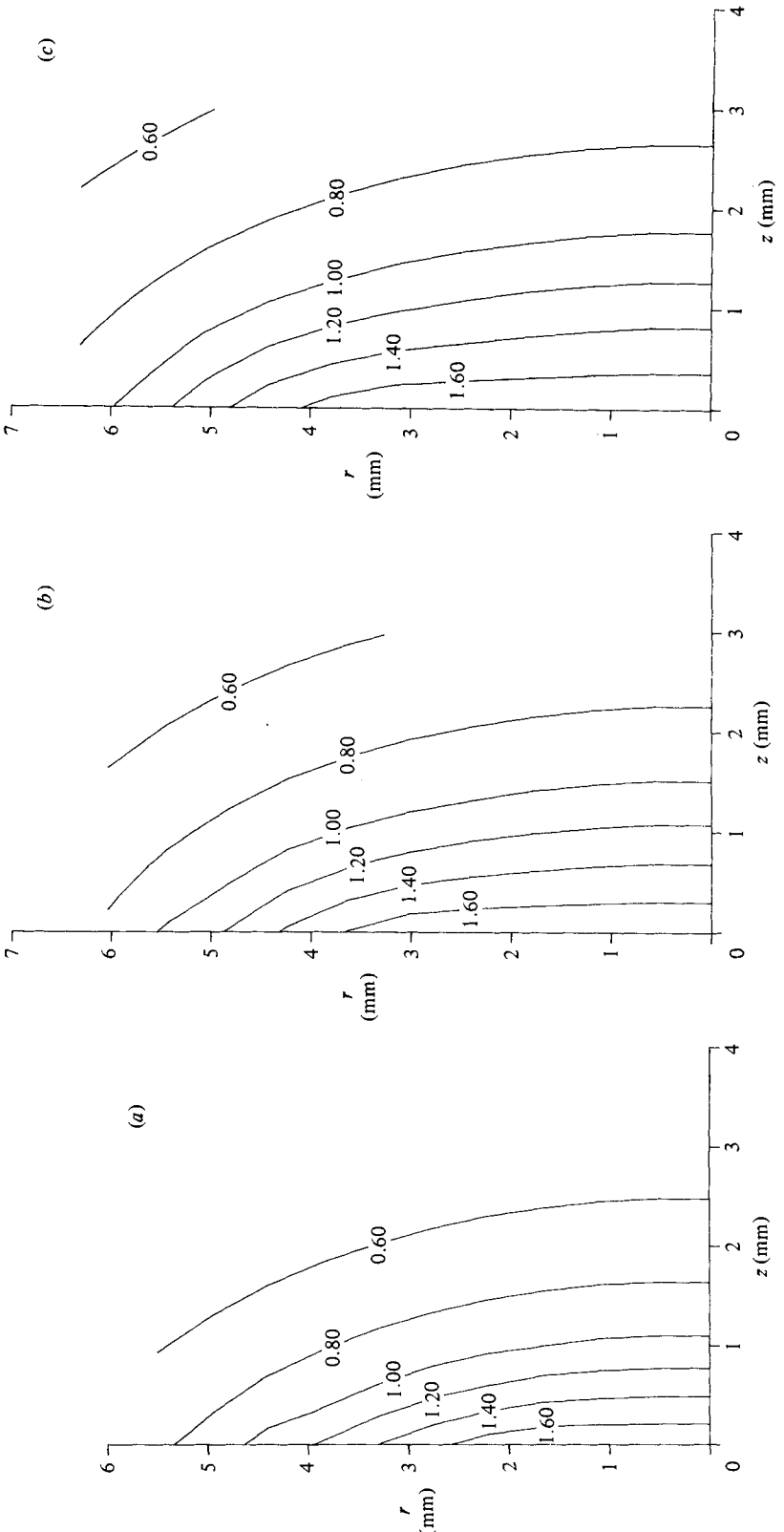

FIGURE 4. Temperature profiles in the case of combined buoyancy and electromagnetically driven flow (normal mode): (*a*) at *t* 2.5 s; (*b*) 5 s; (*c*) 8 s. The numbers on the curves represent the ratio of actual temperature/characteristic temperature.

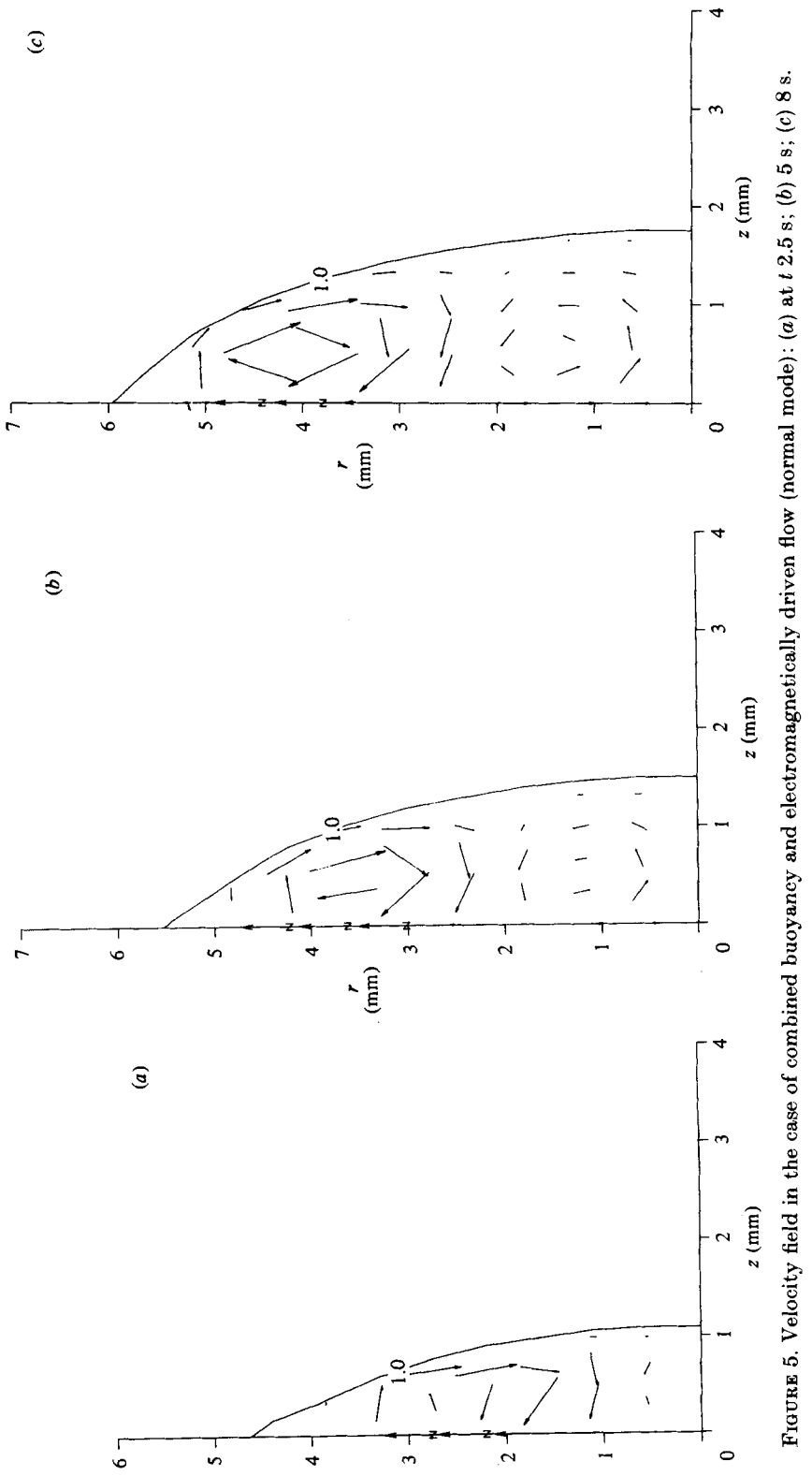

FIGURE 5. Velocity field in the case of combined buoyancy and electromagnetically driven flow (normal mode): (*a*) at *t* 2.5 s; (*b*) 5 s; (*c*) 8 s.

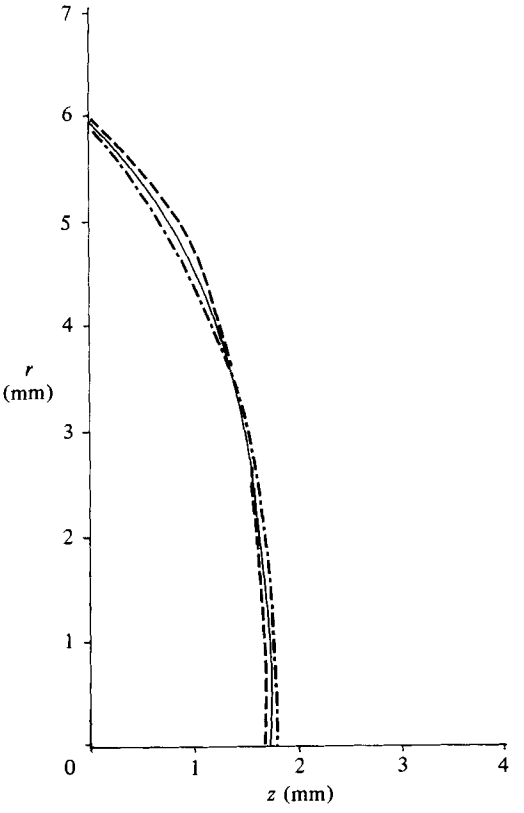

FIGURE 6. Shape of the weld pool corresponding to the normal mode of operation after 8 s of welding. The dotted line corresponds to the pure conduction, the dashed line corresponds to the buoyancy-driven flow, and the solid line corresponds to combined buoyancy and electromagnetically driven flow.

discernible, indicating that buoyancy forces play an important role at a distance from the axis of symmetry, while the rather weaker counterclockwise circulation pattern in the centre of the weld pool is attributable to electromagnetic forces, which appear to gain strength with the growth of the weld pool. These findings are consistent with the order-of-magnitude analysis presented earlier in this section.

These double circulating loops have been predicted and also observed in electroslag refining (Choudhary & Szekely 1980, 1981*a*,*b*).

It should be noted that while in principle double-loop circulation systems could be produced by buoyancy forces alone, in the present study computed results, which are not reproduced here, have clearly shown that buoyancy forces resulted in a single-loop circulation system, while the combined effect of electromagnetic and buoyancy forces could, under certain circumstances, result in a double-loop circulation.

At this stage it is instructive to compare the predictions made for the shape of the weld pool, based on

(*a*) conduction only,

(*b*) natural convection, and

(*c*) on the combined action of electromagnetically and buoyancy-driven flows.

This is done in figure 6, and it is seen that the profiles predicted on the basis of these three mechanisms are essentially the same. This behaviour is fully consistent with

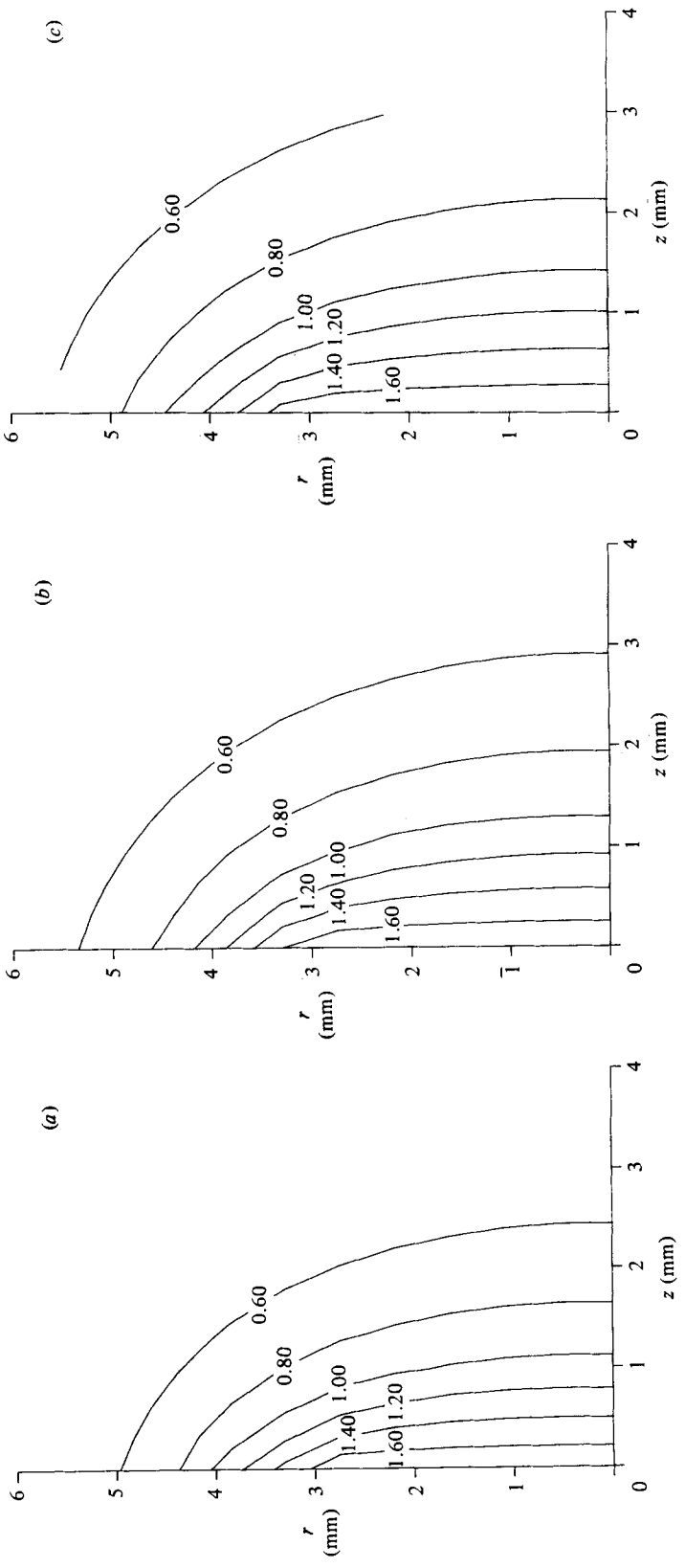

FIGURE 7. Temperature profiles for pure-conduction heat transfer (cathode spot mode of operation): (*a*) at t 2.5 s; (*b*) 5 s; (*c*) 8 s. The numbers on the curves represent the ratio of actual temperature/characteristic temperature.

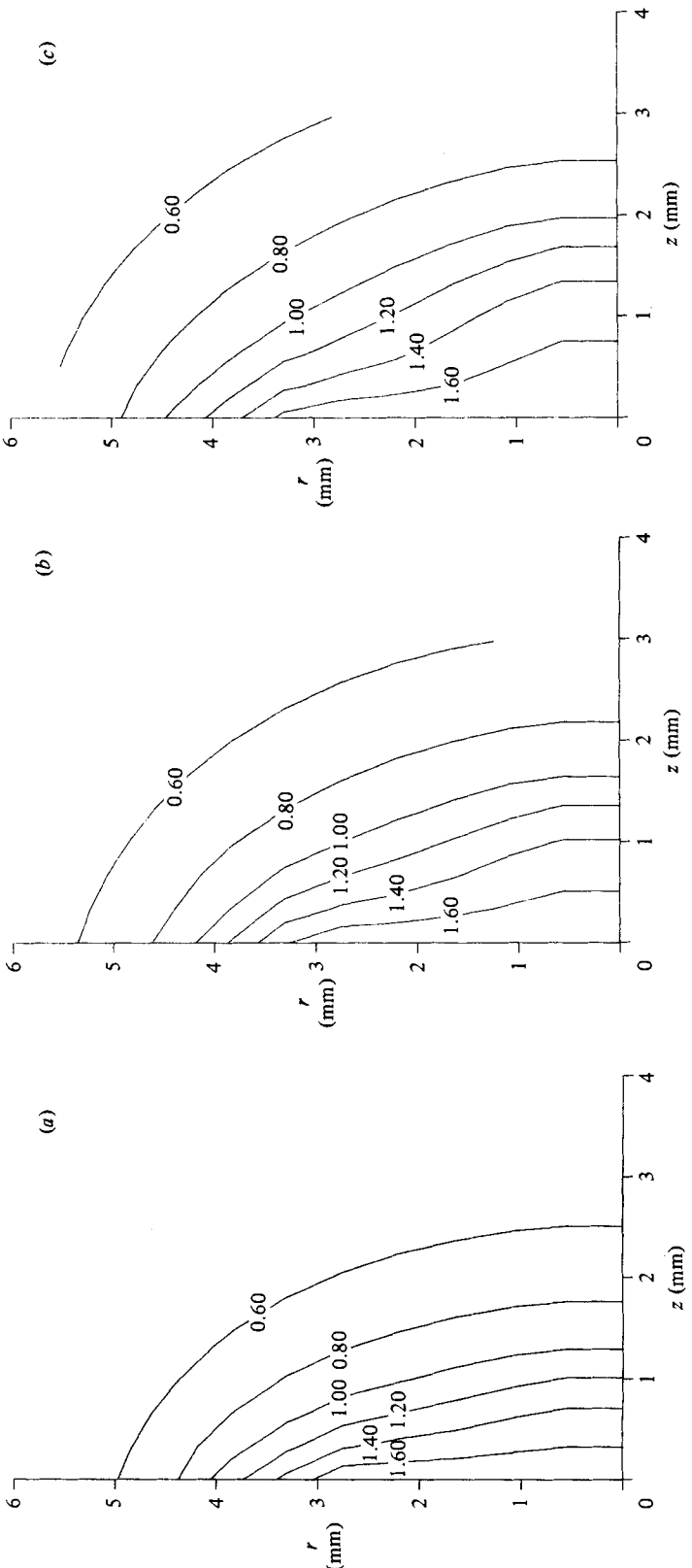

FIGURE 8. Temperature profiles in the case of combined buoyancy and electromagnetically driven flow (cathode spot mode of operation): (*a*) at 2.5 s; (*b*) 5 s; (*c*) 8 s. The numbers on the curves represent the ratio of actual temperature/characteristic temperature.

the previously presented discussion in which the order-of-magnitude analysis has shown, that, for the input parameters chosen, convective heat transfer does not play an important role.

Calculations were also carried out by neglecting the transient term in the vorticity-transport equations; that is, by making the quasi-steady-state approximation. For the normal mode of operation the results thus obtained were indistinguishable from those developed by the solution of the full transient equations. This finding again is consistent with the order-of-magnitude analysis, presented above, showing that the time derivative of the vorticity was significantly smaller than the other terms in the vorticity-transport equation.

It has been remarked previously that the proper scale for the velocity will depend on the quantity $Re\,A^2$. The consideration of the computed velocity fields, as given in figure 5, enables one to test this contention.

Examination of the velocity fields has shown that

$$U_{R,0} \sim \frac{g\beta\,\Delta T L_Z^3\,\rho}{\mu L_R}$$

suggested by (15), notwithstanding that the criterion $Re\,A^2 \ll 1$ was not satisfied. This may be explained by the fact that the flow field was dominated by buoyancy forces, which in turn were confined to a relatively small region at the outer edge of the pool. It follows that the correct linear scale for the Reynolds number would have to be smaller than the pool radius.

4.2. *The cathode spot mode of operation*

Under these conditions, defined in table 2, both the heat flux and the current are sharply focused.

Figures 7(*a*)–(*c*) show the computed temperature profiles in the absence of convection.

Figures 8(*a*)–(*c*) show the computed temperature profiles for the case where both buoyancy and electromagnetically driven flows have been taken into account, while the corresponding velocity profiles are seen in figures 9(*a*)–(*c*).

Inspection of figure 9 shows that in this case the circulation is countercockwise; thus the fluid field is dominated by electromagnetic forces. This behaviour is reasonable on physical grounds, because the strongly divergent current field will generate much stronger electromagnetic forces. Using the parameters defined in the order-of-magnitude analysis, the quantity R defined in (14) was about 3, indicating dominance by electromagnetic forces. In the cathode spot mode of operation, after a certain time a deep pool may develop, with relatively high velocities; then $Re\,A^2 > 1$ and $R > 1$. Under these conditions the convective and the electromagnetic terms will dominate, and thus we may write

$$U_{R,0} \sim \mu L_R \alpha_j^2 \left(\frac{R j_m L_Z C}{L}\right)^{\frac{1}{2}} \pi\rho. \tag{18}$$

A comparison of figures 7 and 8 shows that the predicted pool profiles are rather different. This difference is seen more explicitly in figure 10, which shows the pool profiles, as predicted on the basis of pure conduction, buoyancy-driven convection and for the case where both the electromagnetic and the buoyancy forces have been taken into consideration. It is readily seen that by neglecting the electromagnetically

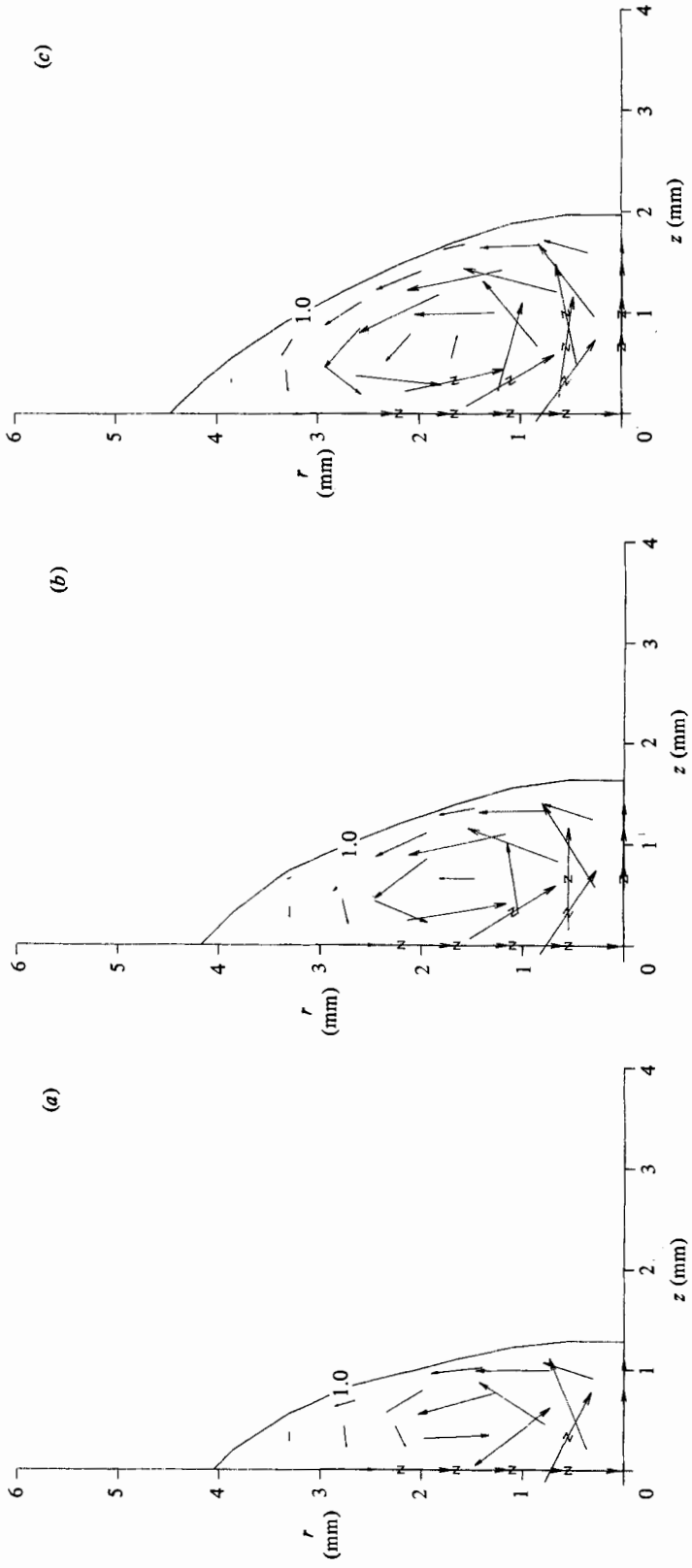

FIGURE 9. Velocity field for combined buoyancy and electromagnetically driven flow (cathode spot mode of operation): (*a*) at 2.5 s; (*b*) 5 s; (*c*) 8 s.

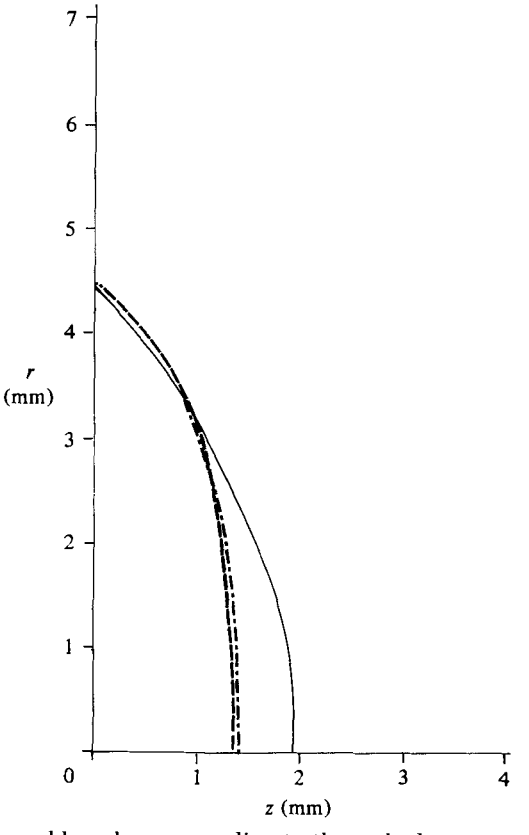

FIGURE 10. Shape of the weld pool corresponding to the cathode spot mode of operation after 8 s of welding. The dotted line corresponds to pure conduction, the dashed line corresponds to the buoyancy-driven flow, and the solid line corresponds to combined buoyancy and electromagnetically driven flow.

driven component one could have seriously underestimated the pool depth in the system.

Invoking the order-of-magnitude analysis for the cathode spot mode of operation, it is readily seen that the parameter $Re\,(L_z/L)\,Pr\,k$ appearing in (3) is now of order unity, indicating that convection does play a significant role, which is precisely the case.

Using arguments that were developed in §4.1, it may be shown that the quasi-steady-state approximation will hold approximately regarding the vorticity transport equation.

Finally it may also be demonstrated, by recourse to (18), that, since $Re\,A^2 > 1$, $U_{R,0}/L_R L_Z^{\frac{1}{2}} \sim$ constant throughout the entire run. Indeed, analysis of figure 9 shows that this relationship is valid to within 10% throughout the duration of the run.

4.3. *Surface-tension effects*

The previously given computed results were obtained on the assumption of zero shear at the free surface. This condition will be met under certain circumstances, while surface-tension gradients could give rise to non-zero shear under yet another set of circumstances. At present there is insufficient knowledge to enable the accurate assessment of surface-tension gradients, so for this reason only an illustration will

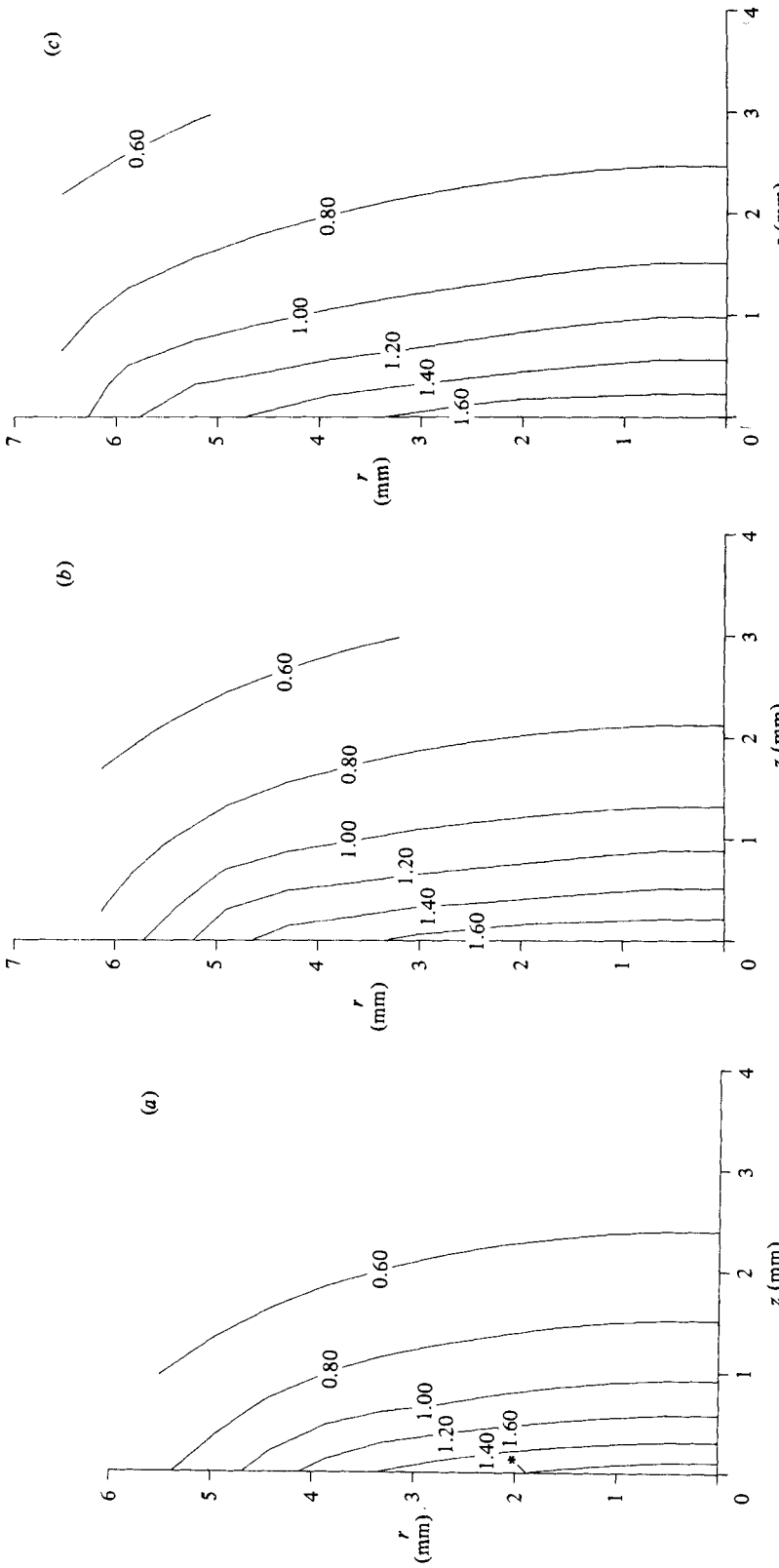

FIGURE 11. Temperature profiles for combined buoyancy electromagnetically and surface-tension-driven flow (normal-mode type of operation, $\partial\gamma/\partial T = -0.01$): (*a*) at 2.5 s; (*b*) 5 s; (*c*) 8 s.

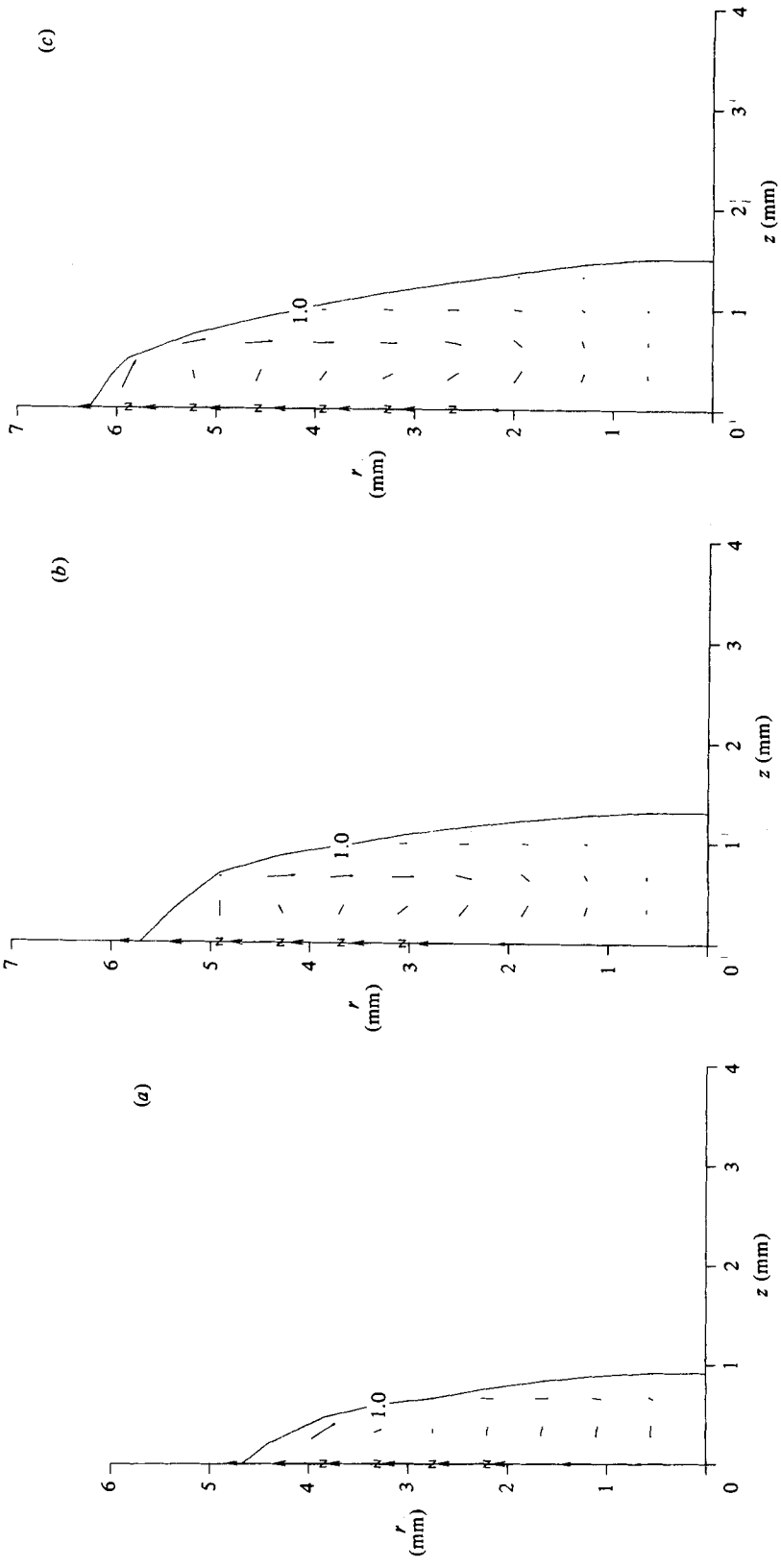

FIGURE 12. Velocity field for combined buoyancy, electromagnetically and surface-tension-driven flow (normal mode of operation, $\partial\gamma/\partial T = -0.01$): (*a*) at 2.5 s; (*b*) 5 s; (*c*) 8 s.

be given of the possible role that surface tension may play in these systems. If the surface tension dominates the flow the characteristic velocity should be evaluated from (5), representing the tangential stress balance at the free surface (Ostrach 1979). When $Re\,A^2 \ll 1$, i.e. for viscous flow, this gives

$$U_{R,0} \sim \frac{\partial\gamma}{\partial T}\frac{\Delta T A}{\mu}. \tag{19}$$

In contrast, when $Re\,A^2 \gg 1$ a boundary-layer flow will occur and the viscous and inertia terms must be of the same order. The boundary-layer thickness δ is the appropriate scale for this latter case, and hence $\delta/L_R = 1/(Re)^{\frac{1}{2}}$ or $\delta/L_Z = 1/A(Re)^{\frac{1}{2}}$. Thus

$$U_{R,0} \sim \left(\frac{(\partial\gamma/\partial T)^2\,(\Delta T)^2}{\rho\mu\,L_R}\right)^{\frac{1}{3}}. \tag{20}$$

When $\delta \ll L_Z$ the aspect ratio $L_Z/L_R = A \gg 1/(Re)^{\frac{1}{2}}$. In evaluating Re (19) or (20) have to be used.

The relative importance of buoyancy and surface tension is usually expressed through the Bond number, defined by the coefficient of the buoyancy term in (3). For the viscous case we have

$$Bo = \frac{Gr\,A^3}{Re}. \tag{21}$$

The analogous parameter for electromagnetic forces may be written as

$$Bo_j = \frac{R_{jm}\,CA^2\alpha_j^4\,L_R^4}{Re\,\pi^2 L}. \tag{22}$$

It may be readily shown that for the parameters chosen in this study

$$Bo \ll 1, \quad Bo_j \ll 1.$$

The quantities Bo and Bo_j may be regarded as modified Bond numbers. Thus we may expect that the flow field would be dominated by surface-tension effects and that these factors would also play a major role in affecting the heat-transfer process.

The computed results to be given in the following have to be regarded as preliminary, because the very steep gradients that existed near the free surface could have introduced some computational inaccuracy.

Figures 11 and 12 show the evolution of the temperature and the velocity profiles for operation with a normal mode (as described) in table 2 and with $\partial\gamma/\partial T = -0.01$, where T is the dimensional temperature.

Inspection of these figures shows quite high outward velocities at the free surface, and the essential absence of significant electromagnetically driven flow. A comparison of the weld-pool and temperature profiles with those given previously in figures 3–10, for identical conditions, but in the absence of surface-tension-driven flows, indicates that for this case the net effect of surface-tension-driven flow was to produce a wider, but shallower, weld pool. This finding is consistent with physical reasoning, since the radial flow at the free surface should broaden the weld-pool dimension, while the relatively stagnant central portion of the pool would lead to a reduced penetration.

Figures 13 and 14 show the time evolution of the temperature and velocity fields, for the normal mode of operation, but now with $\partial\gamma/\partial T = 0.01$.

It should be remarked that a positive temperature coefficient for the interfacial tension would not be feasible on physical grounds for pure materials; however, such

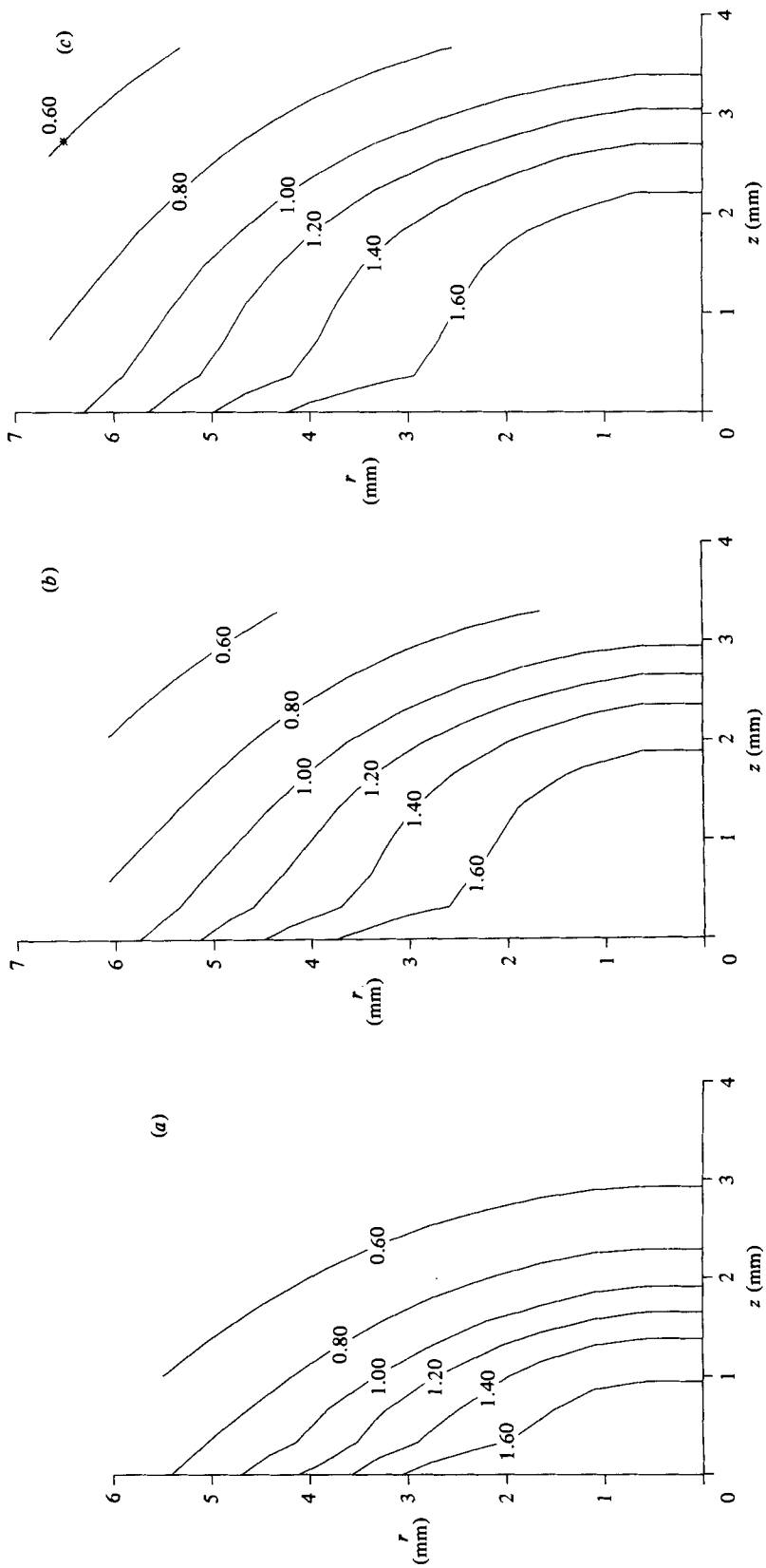

FIGURE 13. Temperature profiles for combined buoyancy, electromagnetically and surface-tension-driven flow (normal-mode type of operation, $\partial\gamma/\partial T = 0.01$): (*a*) at 2.5 s; (*b*) 5 s; (*c*) 8 s.

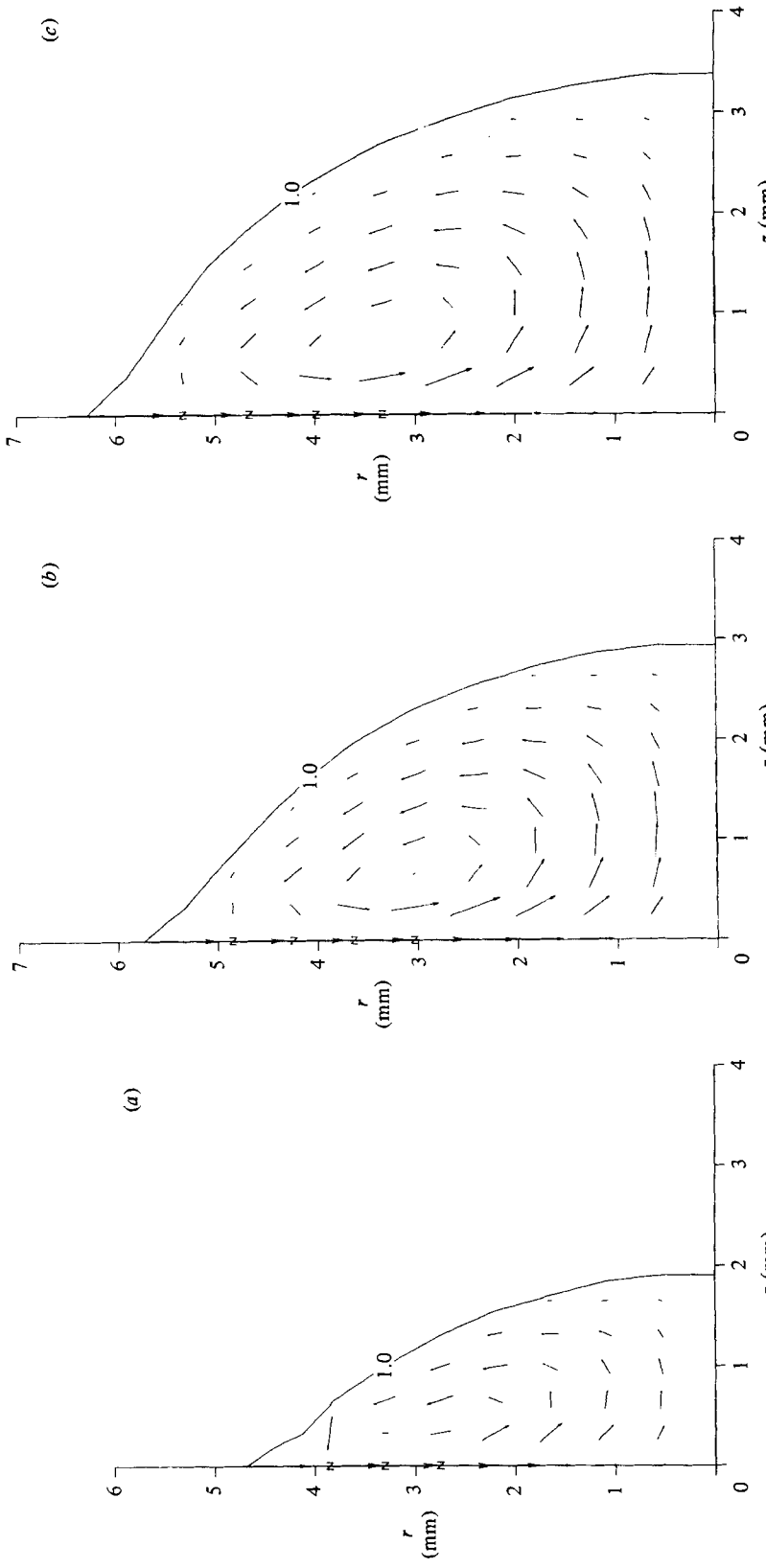

FIGURE 14. Velocity field for combined buoyancy, electromagnetically and surface-tension-driven flow (normal-mode type of operation, $\partial\gamma/\partial T = 0.01$): (*a*) at 2.5 s; (*b*) 5 s; (*c*) 8 s.

behaviour may be found in practice owing to the accumulation of surfactants at the free surface. Inspection of figures 13 and 14 shows a strong counterclockwise circulation pattern, with very high velocities, which is dominated by the combined effect of the surface tension and the electromagnetically driven flow components. The weld-pool shape, involving deep penetration, is consistent with the circulation pattern, which brings the hottest material from the central portion of the free surface, 'straight down' to the bottom of the pool.

It is readily seen from inspection of figures 11–14 that surface-tension-driven flows may have quite a marked effect on both the circulation pattern and on the weld-pool shape, and that these effects deserve further attention.

5. Discussion

A mathematical formulation has been developed to represent the transient behaviour of the fluid-flow field and the temperature field in a liquid pool, which is generated by a spatially variable heat flux and current falling on an initially solid metal block. This physical situation provides a somewhat idealized representation of heat transfer and fluid flow in weld pools.

The formulation was thought to be quite comprehensive because allowance was made for both electromagnetically and buoyancy-driven flows and for the transient nature of the process. Furthermore, the effect of surface tension has also been explored. Previous related studies were concerned with rather more isolated aspects of this problem.

An efficient numerical technique has been developed which enabled the generation of time-dependent solutions for the temperature and the fluid flow fields.

The bulk of the results were obtained for conditions where surface-tension effects were not taken into consideration. It is thought that there may be conditions when this is an appropriate assumption (Heiple & Roper 1982) owing to the accumulation of surfactants or other chemical effects. On commenting on these, an interesting aspect of the results was that the transient nature of the process provided marked changes in the flow patterns. For the particular conditions chosen, initially, for small pool depths the velocity field was dominated by buoyancy forces, giving a clockwise circulation pattern on the right-hand side of the pool. For longer times and larger pool sizes the electromagnetically driven component of the flow became significant and a double-loop circulation pattern was observed. Perhaps the most important finding of this research was that the actual spatial distribution of the current and of the heat flux produced by the arc play a very important role in determining heat flow, the pool profiles and the patterns of convection within the pool.

One set of computed results, obtained for a normal model of operation, as cited by Nestor (1962), produced heat flow, which was not very much affected by convection. This behaviour was consistent with the order-of-magnitude analysis presented in the present paper. The circulation in the pool was dominated initially by buoyancy forces, while electromagnetic forces became important during the latter stages of the process. This behaviour is again consistent both with physical reasoning and the analysis presented. In a physical sense the system is bounded by largely isothermal surfaces, which restrict the domain of buoyancy-driven flows; for longer times, upon increasing the physical scale, electromagnetic forces will become more significant. This is also reflected in the dependence of the quantity R on the pool radius.

The other set of computed results corresponded to a mode of operation (termed cathode spot in practice) where the current and the heat flux were quite concentrated

near the axis of the pool. Under these conditions, the very strongly divergent current path gave rise to much stronger electromagnetically driven flows, which were dominant. In this case, convection also played an important role in affecting the overall heat-transfer characteristics of the system; in particular, in modifying the pool profile. The greater pool depths may be attributable to a combination of factors, including the higher intensity of the heat input near the axis of symmetry and the anticlockwise circulation pattern, which brought hot fluid from the centre of the free surface, down the vertical axis of the pool, in addition to the actually larger fluid velocities encountered in this case. Under these conditions, to neglect the convection heat-flow effects would have introduced a serious error. This behaviour is again consistent with the analysis, which has shown the marked sensitivity of the parameter R on the current distribution; furthermore by scaling the convective terms in the thermal-energy balance equation, convection was found to be significant for such systems in affecting the heat-transfer rate.

A limited number of calculations was also carried out, examining the effect of surface-tension-driven flows. In a mathematical sense this means that the boundary condition specifying zero shear at the free surface was replaced by an expression which related the surface shear to the product of the temperature gradient and the derivative of the surface tension with respect to temperature.

These calculations have shown that surface-tension-driven flows may have a profound effect on weld-pool behaviour. When $\partial\gamma/\partial T$ is negative the resultant radial outflow of hot material from the centre will produce in a wider but shallower weld pool. Extrapolating this behaviour, large negative values of $\partial\gamma/\partial T$ may cause extremely shallow weld pools and hence result in defects.

Positive values of $\partial\gamma/\partial T$ may occur in the presence of impurities (Heiple & Roper 1982). The calculations carried out for this condition have shown that the resultant counterclockwise circulation pattern will result in a deep penetration of the weld pool.

It is thus seen that surface-tension effects may be quite significant in producing very high surface velocities and very marked variations in the weld-pool shape, obtained for relatively small changes in the operating conditions. These findings appear to be consistent both with the order-of-magnitude analysis and with experience reported in the welding literature.

The numerical values of the velocities calculated were found to depend quite markedly on the current and heat input distribution and on the pool size; because of these factors a direct comparison with results reported by other investigators is not quite straightforward. It is thought, nonetheless, that the range of the velocities calculated for the larger pool sizes was comparable to those reported by Atthey (1980).

6. Concluding remarks

A formulation has been developed to represent the electromagnetic force field, the velocity field and the temperature field in a metal slab onto which a plasma jet is impinging, thus providing a somewhat idealized model for the TIG welding process.

The formulation is thought to be quite comprehensive, because allowance has been made for the transient nature of the system, with a moving boundary, and for the combined effect of electromagnetic, buoyancy and surface-tension forces. The principal findings of the work may be summarized as follows.

(1) The TIG welding operation is a very complex process, which is affected by a number of parameters, such as transient conduction, buoyancy, electromagnetic and surface-tension forces.

(2) Under certain conditions, such as a broadly distributed heat source ($R < 1$) and in the absence of surface-tension forces ($M = 0$), convection plays a relatively minor role in heat transfer, and thus the system may be adequately modelled by considering conductive heat transfer only.

(3) However, under other conditions, such as sharply focused heat and electric-current sources ($R > 1$) and when surface-tension effects are significant ($Bo, Bo_j \ll 1$), convection may play a very important, indeed dominant, role in determining the weld-pool shape.

(4) The above-noted complexity of the system is likely to be responsible for the apparent lack of success in explaining widely varying weld-pool shapes obtained under seemingly similar operating conditions. Indeed the marked changes produced by surface-tension-driven flows, which may be altered by slight changes in process chemistry, could provide a partial explanation for these phenomena.

(5) Clearly further work would be desirable in exploring additional complexities of these systems, such as flow instabilities, and the two-way interaction between the weld pool and the impinging plasma, brought about by the selective volatilization of some of the weld-pool components. Such work is currently in progress.

The authors wish to thank the US Department of Energy for support of this investigation under Grant De-AC02-78ER-94799.A0003. Thanks are also due to Professor T. W. Eagar for helpful discussions and to Professor S. Ostrach for constructive comments on the manuscript.

REFERENCES

ATTHEY, D. R. 1980 *J. Fluid Mech.* **98**, 787.

BERTRAM, L. A. & ZANNER, F. J. 1981 In *Modelling of Casting and Welding Processes* (ed. M. D. Brady and D. Appelian).

CHOUDHARY, M. & SZEKELY, J. 1980 *Metallurg. Trans.* **11B**, 549.

CHOUDHARY, M. & SZEKELY, J. 1981*a* *Iron Making & Steelmaking* **8**, 225.

CHOUDHARY, M. & SZEKELY, J. 1981*b* *IMM* **20**, 1691.

DILAWARI, A. H., SZEKELY, J. & EAGAR, T. W. 1978 *Metallurg. Trans.* **9B**, 371.

GOSMAN, H. D., PUN, W. M., RUNCHAL, A. K., SPALDING, D. B. & WOLFSHTEIN, M. 1969 *Heat and Mass Transfer in Recirculating Flows.* Academic.

GOURLAY, A. R. 1970 *J. Inst. Maths Applics* **6**, 375.

GOURLAY, A. R. & MCGUIRE, G. R. 1971 *J. Inst. Maths Applics* **7**, 216.

HEIPLE, C. R. & ROPER, J. R. 1982 *Welding J.* **61**, 97s.

LANCASTER, J. F. 1980 *Metallurgy of Welding*, 3rd edn. Allen & Unwin.

NESTOR, O. M. 1962 *J. Appl. Phys.* **33**, 1638.

OSTRACH, S. 1979 In (*COSPAR*) *Space Research 19* (ed. M. Rycroft). Pergamon.

SPARROW, E. M., PATANKAR, S. V. & RAMADHYANI, S. 1977 *Trans. ASME* C: *J. Heat Transfer* **99**, 520.

SZEKELY, J. 1979 In *Rate Processes of Extractive Metallurgy* (ed. H. Y. Sohn & M. E. Wadsworth). Plenum.